Modelling Seismic Hazard for Mines

Aleksander J. Mendecki & Ernest C. Lötter
Institute of Mine Seismology, Australia

Australian Earthquake Engineering Society 2011 Conference
18-20 November Barossa Valley, South Australia

Abstract

Unlike earthquakes, seismic rock mass response to mining can be controlled. Seismic hazard in mines is driven by the volume and the spatial and temporal distribution of rock extraction. To forecast seismic hazard for a given mine layout we need to extrapolate its parameters in the volume mined domain rather than in time.

It is difficult to reconcile the far-field point source model and ground motion recorded away from seismic sources, where details of the rupture process are hidden, with the violent nature of damage resulting from major rockbursts. From linear elastic considerations the rate of stress release with an increase in slip velocity must, at all times, be less than the acoustic impedance, ρv_S. The maximum possible ground velocity is then limited by the bulk shear strength of the rock, σ_{bss}, and may be roughly estimated as $\dot{u}_{max}$ = 0.5 $\sigma_{bss}/\rho v_S$. However if the rate of loading exceeds the rate at which energy can be removed by elastic waves the large strains may have to travel faster than small ones generating extreme ground motion that extends further away from the source.

Seismic networks in mines are not suitable to measure strong ground motion close to excavations. Therefore to assess damage potential to mine infrastructure one needs to model ground motion produced by large seismic events expected in a given area. Preliminary results of 3D finite-difference kinematic modelling applied to complex source mechanisms in the presence of underground excavations are presented. This includes two-fault systems proposed by *Ortlepp*, 1984 and 1997, as well as simulations of surface ground motions in an urban environment. A rotated staggered grid is used as basis for the forward model, which simplifies the implementation of free surface conditions and is more applicable to the highly heterogeneous medium model in mining situations. Even when the static source parameters are kept fixed, there are great differences in resolved ground motions at points of interest under different rupture velocities and slip distributions.

1 Earthquakes vs Mining Induced Hazard

Earthquake driving forces can not be controlled. They are fairly constant and relatively slow compared to changes in stresses induced by mining. This slow loading facilitates the process of self-organisation that leads to a state at which

the system develops reproducible relationships among its distant parts (*Nicolis and Prigogine* 1989; *Rundle et al.* 2002). It is assumed that this growth of long range correlations allows for progressively larger events to be generated. These large events in turn partially de-correlate the system and the process continues (*Sornette*, 2005). In such a case having a sufficiently long catalog of past earthquakes and realistic data on geological structures would give a reasonable indication of future hazard. But the time scales involved here are huge and seismological data is far from adequate. The causative faults are inaccessible and the inferred information about their extent, orientation and properties is sparse.

For systems driven steadily over long periods of time the sequence of record breaking events is a monotonously increasing function of time with decreasing gradient (e.g. *Chandler*, 1952; *Glick*, 1978; *Mendecki*, 2008; *Van Aalsburg et al.*, 2010). Therefore the problem of estimating the maximum possible magnitude of an earthquake in a given area, m_{max}, may be reduced to finding the truncation point of the observed distribution of past events. An obvious estimator here is m_{maxo} - the largest observed event, which will underestimate m_{max}, but the bias should decrease as the size of the data set increases. After correction for the bias (*Robson and Whitlock*, 1964; *Cooke*, 1979; *Kijko*, 2004) the estimated m_{max} is a fraction greater than m_{maxo}. The exponents of the observed power law size distribution of global and regional seismicity are remarkably stable (*Wesnousky* 1999).

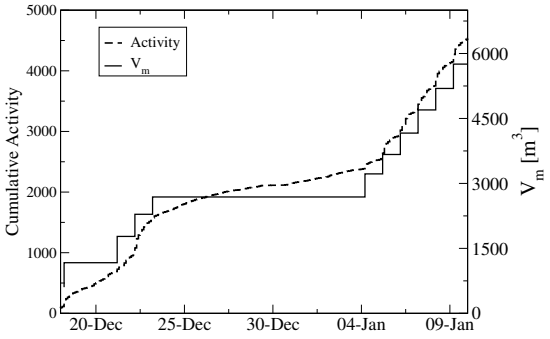

Figure 1: Drop in the rates of seismic activity during 2010 Christmas break in a gold mine in South Africa.

Mining is not a spontaneous process. It induces stresses at a particular place, at a particular time and at a particular rate which are all highly variable compared to the tectonic regime. An average rate of deformation induced by mining is at least two orders of magnitude greater than the average slip rate of tectonic plates. The instantaneous closure after production blasts of tabular reefs in a deep South African gold mine can be as high as 1 cm, followed by a steady state closure at the rate of 1.5 cm/day for a number of days (*Malan*, 1999). Underground openings facilitate deformation and relaxation of stresses, hence aftershock sequences, even after larger events in mines, continue only for few days - not for years.

Given some short time delay for rock mass excitation and relaxation, the bulk of seismic activity in mines starts with rock extraction, increases with the extraction ratio of the ore body and stops with cessation of mining. Figure 1 presents an example of seismic rock mass response to the 11 days production break over December and January 2010. Large scale mining taking place over

number of years, however, alters the regional stress regime and may induce earthquake type events which are less correlated with the recent mining, e.g. Belchatow $m4.6$ in 1980 (*Gibowicz et al.*, 1981), Newcastle $m5.6$ in 1989 (*Gibson et al.*, 1990; *Klose*, 2007), Kalgoorlie $m5.1$ in 2010 (*Hao*, 2010; *Cranswick*, 2011), Welkom $m5.0$ in 1976 (*Van Aswegen*, 1990; *Ortlepp*, 1997) and Klerksdorp $m5.3$ in 2005 (*Durrheim et al.*, 2006).

Seismic events in mines can be considered as small earthquakes, therefore their magnitude should scale with energy, E, and potency - the product of an average slip and source area - $P = \bar{u}A$, as $m \propto \log E \propto \log P$, as oppose to moderate to large earthquakes where scaling is $m \propto 2/3 \log E \propto 2/3 \log P$ (*Kanamori and Anderson*, 1975; *Mendecki*, 1993 Figure 1.2; *Ben-Zion and Zhu* 2002). Mining districts are not well covered by the national seismological networks and it is difficult to calibrate their magnitude scales. Since the accuracy of magnitude determination in mines is 0.25 to 0.5 unit, one can use the relevant moment or potency-magnitude scale, e.g. $m = \log P + 0.32$, given by *Gibowicz* (1975), or simply use $\log P$ as a measure of magnitude.

The catalogue of mine seismic data in most cases is adequate and the geology of the ore body and the surrounding rock mass is well explored. Past data is useful to compare seismic rock mass response to different mining scenarios but, because of the intermittent nature of loading, is not the best indication of future hazard. To forecast future hazard we need to take into account future mining (*Mendecki*, 2008).

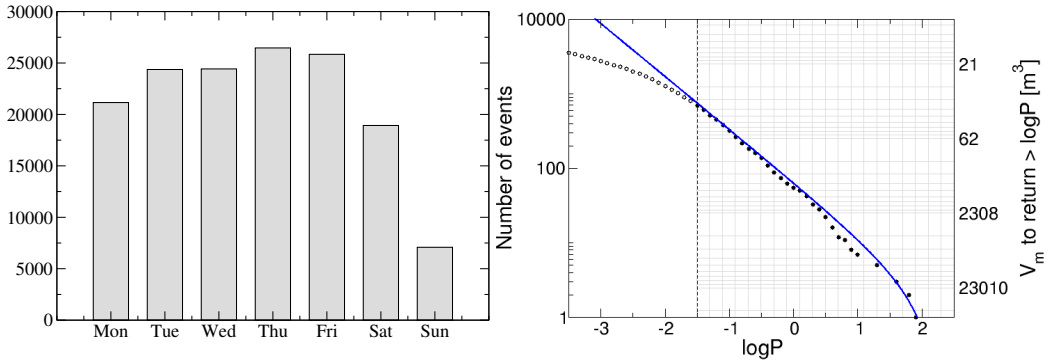

Figure 2: Day of week distribution of seismic activity over 3 years in a mine with limited production on Saturdays and no production on Sundays *(left)*. Potency-frequency plot over the same period of time with recurrent volume mined *(right)*.

Figure 2 (left) shows day of week distribution of seismic activity over 3 years in a mine with limited blasting on Saturdays and no production on Sundays and Figure 2 (right) shows the potency-frequency distribution of the same data set. Note that the recurrence time at Figure 2 (right) has been replaced by the average volume mined to produce an event above a certain size. The mean inter event time for events with $\log P \geq 0.5$ is 2.96 days with a standard deviation of 4.54

days. This gives a coefficient of variation, C_v = 4.54/2.96 = 1.53. The mean inter event volume mined V_m is 655 m^3 with a standard deviation of 298.76 m^3, which gives C_v = 0.45. The higher the coefficient of variation the more variable, or clustered, is the process. The uniform distribution has zero standard deviation therefore C_v = 0, a quasi-periodicity is characterized by 0 < C_v < 1 and clustering by C_v > 1. It is therefore more informative to quote an average volume to be mined to produce a given seismic activity rather than the recurrence time. Large events in mines tend to be more randomly distributed and both the volume mined and recurrence time have a similar distribution.

Ground motion in mines is recorded only at a limited number of sites and frequently far from active excavations where instrumentation is difficult. Most systems in mines do not measure ground motion at the skin of excavations. They are designed to locate events and to estimate their source parameters. For this reason seismic sensors are placed in boreholes, away from excavations, to avoid the very site effects that amplify ground motion. As a result seismic hazard analysis in mines is limited to estimates of probabilities of occurrence of seismic events above a certain magnitude.

The probability that an event will exceed potency P while mining the volume of rock $V_{\Delta m}$ over time ΔT into the future can be given as

$$\Pr\left[\geq P, V_{\Delta m}\right] = 1 - \left(\frac{1}{1 + \Pr\left(> P, \alpha(V_{\Delta m}), \beta(V_{\Delta m})\right)}\right)^{n[\alpha(V_{\Delta m}), \beta(V_{\Delta m})]+1}, \quad (1)$$

where $n[\alpha(V_{\Delta m}), \beta(V_{\Delta m})]$ is the expected number of events above the threshold magnitude P_{min}, the $V_{\Delta m}$ and $\Pr\left(> P, \alpha(V_{\Delta m}), \beta(V_{\Delta m})\right)$ is the expected survival function of the assumed potency-frequency distribution with parameters α, that measures the activity rate, and β which is the exponent, both functions of the volume already mined and to be mined. Equation (1) takes into account the inherent uncertainty in the rate of occurrence of seismic events (*Benjamin*, 1968; *McGuire*, 1977; *Campbell*, 1982).

The most frequently used survival functions to estimate seismic hazard are: (1) the open-ended power law with no limit on maximum event size, (2) the upper-truncated power law with hard limit P_{max} and (3) the Gamma-type which is the product of the open-ended survival function and an exponential taper which constitute a soft limit P_{max}, above which the probability decays quickly but is finite. The sequence of the record highs in mines is jerky, therefore for short term hazard it is more useful to define P_{max+1} - the next record breaking event, as opposed to the largest ever possible. The correcting term here can be $\log P_{max+1}$ = $\log P_{maxo}$ + $\max\left(\Delta \log P_{maxo}\right)$, where the $\max\left(\Delta \log P_{maxo}\right)$ is the maximum jump in the logarithms of the observed series of record potencies (*Mendecki*, 2008). Since mining scenarios may change, it is advisable to select the past data that is most relevant to future mining. In mines α tends to increase and β tends to decrease as extraction ratio increases - therefore they are functions of the volume mined V_m. By extrapolating the observed relationship between α, β and the volume mined, or time, see dotted lines in Figure 3, we can forecast future hazard for different production scenarios using equation (1).

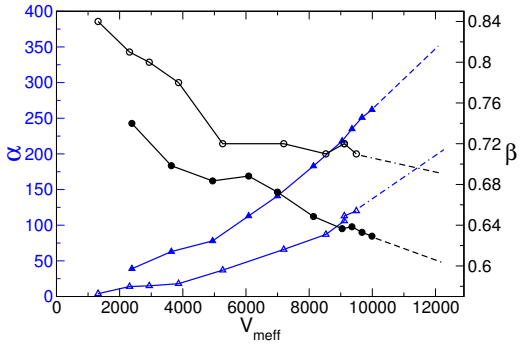

Figure 3: Parameters α (triangles) and β (circles) versus volume mined for two South African mines.

All else being equal, seismic hazard in mines is driven mainly by volume and the spatial and temporal distribution of rock extraction. In general, mining scenarios that induce spatial and temporal heterogeneity, or disorder, tend to de-correlate the system and are less likely to generate larger dynamic instabilities (*Mendecki*, 2005). Therefore, unlike earthquakes, seismic hazard in mines can largely be controlled. Introducing stabilising pillars, backfill, changing the sequence of mining or reducing the extraction ratio may all mitigate seismic response (e.g. *van Aswegen and Mendecki*, 1999; *Handley et al.*, 2000; *Capes*, 2010).

2 Near-Source Ground Motion

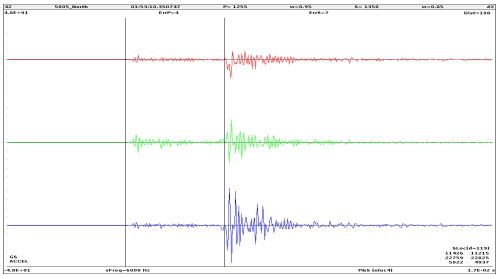

Figure 4: Peak accelerations of 53 m/s^2 at 1550 Hz (u = 5.6·10^{-7}m) recorded 108 m from $\log P$ = -1.3 event at Ridgeway mine. The sampling rate is 6 kHz, the resonance frequency of the sensor is 15 kHz and the response of its internal filter drops to -3 dB at 2.3 kHz which marks the upper limit of the usable frequency band.

The maximum ground motions that can be experienced at a site close to source are controlled by the maximum slip velocity, the interaction of radiation from different parts of the source and from different travel paths, and by the site effects. Severe damage to underground excavations in mines is observed mainly near the source area. Minor damage can be caused by ground velocities as low as few cm/s. Falls of ground in poorly supported areas can be triggered by ground motion as low as a few mm/s. There is a weak correlation between damage and the observed peak acceleration. Small events may generate large accelerations but at high frequencies, therefore they produce little deformation, $u \propto \ddot{u}/f^2$, see Figure 4.

The ground velocity at source is controlled by the maximum stress at source which, in turn, is limited by the strength of the rock mass. Consider a small piece of ground attached to an infinite source bounded across a plane by the extent of a rupture propagating with velocity v_r over small increment of time Δt, and away from the source plane by the extent of the propagating S-wave with velocity v_S,

see Figure 5. If the applied effective stress σ_{eff} available to accelerate the two sides of the source is released instantaneously then the rock mass acceleration, $\ddot{u}$, and velocity, $\dot{u}$, can be derived from $\ddot{u} = F/m$, where here force $F = \sigma_{eff}(v_r\Delta t)^2$ and mass $m = \rho(v_r\Delta t)^2 v_S \Delta t$, therefore

$$\ddot{u} = \frac{F}{m} = \frac{\sigma_{eff}}{\rho v_S \Delta t} = \frac{\sigma_{eff}}{\mu \Delta t} v_S; \quad \Longrightarrow \quad \dot{u} = \frac{F\Delta t}{m} = \frac{\sigma_{eff}}{\rho v_S} = \frac{\sigma_{eff}}{\mu} v_S, \tag{2}$$

where $\mu = \rho v_S^2$ is rigidity and ρv_S is the shear wave impedance.

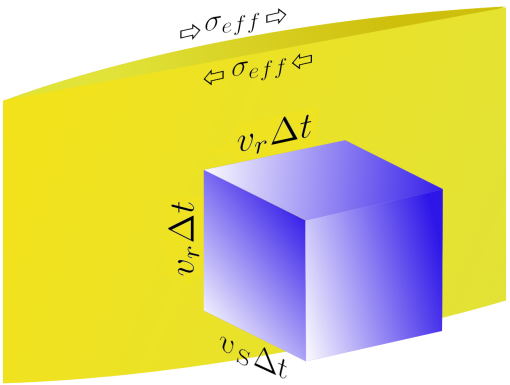

Figure 5: Sketch of a volume of ground attached to a moving fault.

According to the above equations: (1) Rock strength does not limit peak acceleration. For small Δt (at high frequencies, $1/\Delta t$) there is practically no limit on peak ground acceleration. Fracture in a continuum may produce a steep change in velocity which results in high acceleration at high frequencies (*Andrews et al.*, 2007). (2) The ground velocity will always be much smaller than the rupture velocity because the effective stress is much smaller than the shear modulus. (3) Rock strength limits ground velocity, which does not depend on frequency. (4) Ground velocity at source does not depend on magnitude.

For a finite source of size $2r$ with instantaneous stress release the effects of the edges of the crack will abate the ground velocity with time. For a simple taper, $\exp(v_S t/r)$, given by *Brune* (1970), integration of equation (2) over process time, r/v_S, gives the average ground velocity $\langle\dot{u}\rangle = 0.63\ \sigma_{eff} v_S/\mu$ (*Kanamori*, 1972). The near source ground velocity for a finite source and finite rupture velocity for different source models are quoted in Table 1.

Table 1: Models of near-source ground velocity as a function of rupture velocity

Model/Author	$\langle\dot{u}\rangle$	for $v_r = 0.75 v_S$
Bilateral rupture (*Burridge*, 1969)	$\langle\dot{u}\rangle = \sigma_{eff}/\left[\rho v_S\left(1 + v_S/v_r\right)\right]$	$\langle\dot{u}\rangle = 0.43\sigma_{eff}/\rho v_S$
Dynamic cohesive rupture (*Ida*, 1973)	$\langle\dot{u}\rangle = \sigma_{eff} v_r/\left(\rho v_S^2\right)$	$\langle\dot{u}\rangle = 0.75\sigma_{eff}/\rho v_S$
Dynamic rupture scaling (*McGarr and Fletcher*, 2001)	$\langle\dot{u}\rangle = 0.8\sigma_{eff}/\left[\rho v_S f\left(v_r\right)\right]$	$\langle\dot{u}\rangle = 0.36\sigma_{eff}/\rho v_S$

The effective stress cannot be measured directly but different approximations can be made. One option is to assume that σ_{eff} is equal to the bulk shear

strength of the rock within the volume of interest, which for most hard rocks varies between 40 and 80 MPa. An intact rock may be considerably stronger. If a reliable data base is available one can also use the maximum stress drop derived from recorded waveforms, which in South African gold mines varies between 30 and 60 MPa. According to equations quoted in Table 1 for σ_{eff} = 50 MPa, μ = 30 GPa, v_S = 3300 m/s and v_r = 0.75 v_S the estimates of the near source ground motion would vary between 2.0 m/s and 4.0 m/s.

An average ground velocity at source can also be estimated from $\langle \dot{u} \rangle = \bar{u}/(2\tau)$, where $\bar{u}$ can either be observed in the field or estimated from the scaling relation, e.g. $\bar{u} = 0.00225\sqrt[3]{P}$ (*Somerville et al.*, 1999), and τ is the rise time taken from the recorded waveforms. The division by a factor of 2 comes from the fact that the near-source ground velocity is equal to half of the slip velocity v_{slip} - the velocity of one side of the source with respect to the other.

In mine seismology the issue of the maximum possible ground motion within the source volume is debatable. Extreme damage experienced during shear-type events cutting through pristine rock where no discernible planar weaknesses existed before implies ground motions well above the accepted 3 m/s limit (see *Ortlepp*, 1984, 1997, 2006). During such events the surrounding rock is shattered into small fragments and pulverized, with particles less than 25 μm in size, and hydraulic props punched deep into the quartzite foot-wall (*Ortlepp et al.*, 2005; see also *Sammis and Ben-Zion*, 2008; *Yuan et al.*, 2011). These events might impart extreme ground motions in the form of localised, directional and focused shock waves into the surrounding rock, as illustrated in Figure 6.

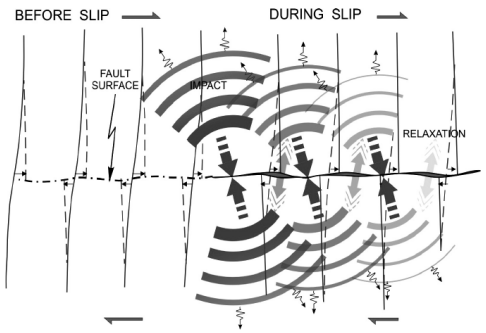

Figure 6: Mechanism for creating extreme compressions and rarefactions along a non-smooth fault surface and generating localised, focused strong ground motions (*Ortlepp et al.*, 2005).

Equations (2) and in Table (1) are applicable when the rate of stress release with an increase in slip velocity is, at all times, less than the shear wave impedance, $d\sigma_{eff}/dv < \rho v_S$. Slip rates given by these equations may underestimate strain rates at the edges of the moving source. If the rate of loading exceeds the rate at which energy can be removed by elastic waves the system is no longer linear. To remove this excess energy the large strains needs to travel faster than small ones - the particle velocity exceeds the shock wave velocity (*Knopoff and Chen*, 2000). This is also what happens during super-shear rupture when the crack tip is moving faster than the S-wave velocity (e.g. *Weertman*, 1969; *Burridge*, 1973; *Savage*, 1971; *Andrews*, 1976; *Olson and Apsel*, 1982; *Archuleta*, 1984; *Spudich and Cranswick*, 1984; *Dunham*, 2007; *Lu et al.*, 2010).

3 Modelling Ground Motion in Mines

Modelling of ground motions in an elastic medium is governed by the equations of motion, i.e. the momentum conservation equations and stress-strain relations

$$\rho\ddot{\mathbf{u}} = \nabla \cdot \boldsymbol{\sigma} + \mathbf{f}; \quad \sigma_{ij} = c_{ijkl}\epsilon_{kl} \tag{3}$$

where the elasticity tensor c_{ijkl} can be parametrised for isotropic media by the two Lamé parameters λ and μ. This parametrisation leads to the equation

$$\boldsymbol{\sigma} = \lambda\nabla \cdot \mathbf{u}\mathbf{I} + \mu(\nabla\mathbf{u} + (\nabla\mathbf{u})^T) \tag{4}$$

While analytical solutions exist for homogeneous medium (constant density ρ and material parameters λ and μ), to model a heterogeneous mine model that may contain free surfaces, caves, stopes and other material contrasts, a numerical solution is needed.

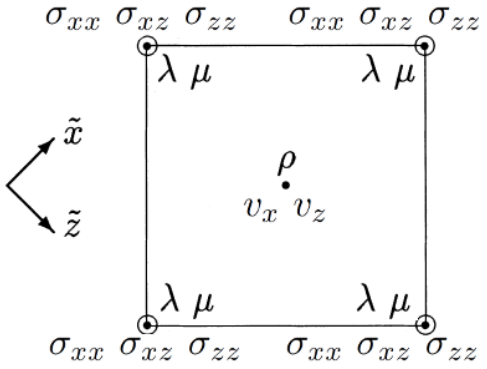

Figure 7: Elementary (2D) cell for velocities and stresses in rotated staggered grid scheme.

A numerical solution of the 3D wave equation is achieved by finite difference modelling. As a first step, partial derivatives in Equation 3 are replaced by numerical first, second or fourth order estimates obtained by a Taylor expansion truncated after the desired number of terms. The decision on where on a finite difference grid to place spatially dependent material properties (ρ,λ and μ) and physical quantities (v_i, σ_{ij}) constitute a choice between various staggered grid schemes. A fourth-order in space scheme is described in *Graves* (1996).

Another scheme is introduced by *Saenger and Bohlen* (2004) which represents the finite difference grid as a rotated grid (Figure 7), with the advantage that all material properties and physical quantities are placed within one elementary grid cell from point values being updated. This allows for the accurate modelling of elastic waves traversing material contrasts, cracks or free surfaces without the need to explicitly implement boundary conditions.

Performing forward modelling of a seismic source using the finite difference method thus firstly requires an accurate description of the elastic medium, which is done by assigning values to the density ρ and material parameters λ and μ at each grid point. Moreover, absorbing boundary conditions on the model domain needs to be added, either by following the A1 absorbing boundary condition of *Clayton and Engquist* (1977) that assumes planar waves, or an attenuating shell around the model that simulates inelastic attenuation. It reduces the influence of non-physical wave reflections off the side of the finite difference model.

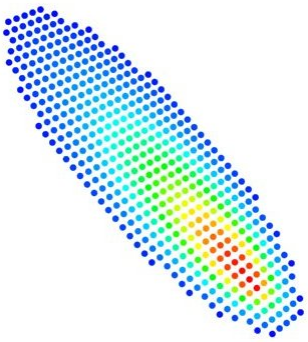

Figure 8: An extended source built from a distribution of point sources.

Inserting one or multiple point sources into a model is conveniently done by applying time dependent body forces using the last term of Equation (3). These force representations is convenient in the staggered grid of simple moment sources with arbitrary mechanisms (*Graves*, 1996).

Modelling a finite source on a finite difference grid is done by superposition of the wave fields from by multiple point sources. These point sources represent point-like parts of the extended source. The seismic potency of the finite source is the sum of the potencies of the constituent point sources, and it is expected that these point sources will have similar principal axes, but may vary in magnitude, as not all parts of the source will experience the same net displacement.

Figure 8 demonstrate such a simple scheme with colours proportional to the final displacement experienced by each point. At the edge of this elliptical source, displacement tends towards zero (blue), while maximum displacement occurs at an off-center point on the principal axis of the source ellipse.

When building a kinematic model of an extended source, the consistency of this set of source parameters and time histories for each point of the fracturing fault is very important. Two features of seismic sources that enforce strong constraints on the possible distributions of these parameters are self-similarity of the final slip distribution and the expected characteristics of the high frequency part of the displacement spectrum as seen in the far field. These consistency constraints on a set of point sources must ensure smooth and monotone slip histories for all parts of the source, while staying physically reasonable.

To provide explicit constraints on the parameters controlling the rupture, the kinematic k-square earthquake source model of *Herrero and Bernard* (1994) can be used. This model yields ω^{-2} far field radiation and k^{-2} slip distribution, meaning that spectral amplitudes of the final slip distribution decay as a power of 2. The idea is, instead of describing the distribution of slip on a fault, rather to describe its Fourier transform. Then the same type of Fourier transform produces similar slip distributions for faults with different dimensions. The k-square model thus represents final displacement at (x, y) on the fault as

$$u(x,y) = \int\int D(k_x,k_y)e^{i(xk_x+yk_y)}dk_xdk_y \tag{5}$$

where $D\left(k_x,k_y\right) = \exp\left[i\Phi\left(k_x,k_y\right)\right] / \sqrt{1+\left[\left(k_x/k_c\right)^2+\left(k_y/k_c\right)^2\right]^2}$, with the function $\Phi(k_x,k_y)$ in the Fourier transform being a random phase. For large values of the wave-number, the Fourier transform decays as the inverse of the square. An

extended source is then constructed by distributing its total seismic potency over the sub-sources, proportional to the modelled permanent displacement at their positions from the k-square model. For sub-source i, we thus obtain $P_0^i = u_i \triangle A$ with the areas of all sub-sources the same due to the constant gridding. Similarly, rise times over different parts of the source are chosen to be proportional to the final slip, thus $T_i = T^{max} \frac{u(\xi_i,\eta_i)}{u_{max}}$ where T^{max} is a chosen rise time corresponding to the sub-source with maximum final displacement.

The slip velocity time-function of a sub-source determines the high frequency behaviour of the amplitude spectrum in the far field. *Beresnev and Atkinson* (1997) have proposed a simple model of a slip velocity time function which leads to a far field displacement spectrum adhering to ω^{-2} decay. The parametrisation of the source time function $\nu\left(t;\tau,\zeta\right) \simeq t \exp\left(-2t/\tau\right)$ allows us to model our chosen rise time for the extended source by choosing $\tau = \frac{1}{2}T^{max}$.

To choose initiation times t_0^i for sub-sources, consider that these must coincide with the time when the rupture front reaches the location of the sub-source. A rupture propagation model thus needs to be imposed in order to determine the initiation times for all sub-sources and hence complete the kinematic model of the extended source. If the simple assumption is made that rupture speed is faster when parallel to slip and slower when orthogonal to slip, we obtain an extended source in the shape of an ellipse, with eccentricity determined by the ratio of these two orthogonal rupture velocities. This is the scenario illustrated by Figure 8.

The initiation times can be calculated by integrating the rupture propagation velocity along the line that connects the sub-source with the hypocenter. Now, the ground motion experienced at a site is controlled by the maximum velocity of deformation at the seismic source (slip velocity), by the interaction of radiation from different sub-sources from different travel paths and by site effects.

3.1 Extended sources in heterogeneous media

Displacement on a fault originates at the focus, and propagates towards its edges. As the focus is not necessarily in the center of the fault, much of the propagation is unidirectional. To examine the extreme ground motions that can be caused at points of interest specifically in the direction of rupture propagation, we modelled two similar extended sources based on the same k-square slip distribution, but with distinct rupture mechanisms. These rupture mechanisms are: $v_r = 0.9v_S$ for sub-shear rupture process and $v_r = \sqrt{2}v_S$ for super-shear process where rupture propagates faster than S-wave velocity. Also present in this model is a tabular stope that causes reflections and partly obstructs waves from directly travelling to the upper part of the rock mass.

Snapshots of the seismic wave field are shown in Figure 9 and 10. From Figures 9 and 10 (for which corresponding frames refer to the same points in time), it is clear from inspection of the wave field that rupture progresses faster in the super-shear case and that a Mach cone evolves (see Figure 10 frame 4).

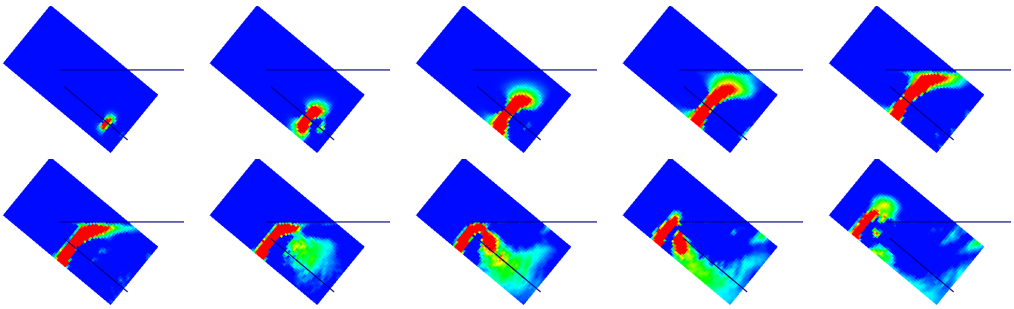

Figure 9: Snapshots in section view of subsequent time steps in a sub-shear rupture process, chronologically from left to right, top to bottom.

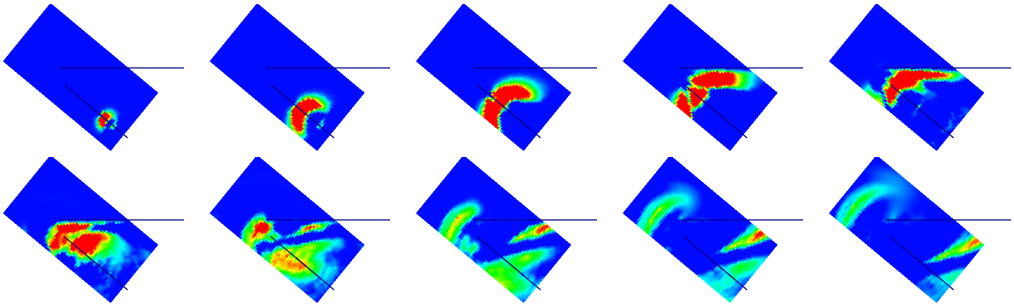

Figure 10: Snapshots in section view of subsequent time steps in a super-shear rupture process, chronologically from left to right, top to bottom.

3.2 Complex sources in heterogeneous media : Ortlepp source

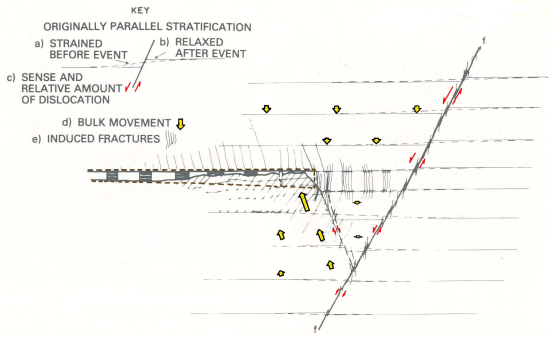

Figure 11: Strike section through a stope showing a double source mechanism conceptualised by *Ortlepp*, 1984 and *Ortlepp*, 1997.

We model a complex source model conceptualised by David Ortlepp and described in *Ortlepp* (1984) and *Ortlepp* (1997) page 63 caption (e), see Figure 11. It is a superposition of two rectangular extended faults, each of which is similar to the single fault sources described in the previous section. The first fault is further away from the stope and it induces rupture on the secondary fault that interacts with the stope. Here we assume that the second rupture is induced by the first one almost immediately.

Due to the freedom available to place sub-sources on the finite difference grid, we are now able to independently choose both the orientations of these faults and the velocity of rupture propagation, v_r. In particular, this

allows modelling of the first (initiating) fault to have sub-shear rupture velocity ($v_r < v_S$) and the second (primary) fault to have super-shear rupture velocity ($v_r > v_S$). In Figure 12 the rupture and slip histories of such a scenario are illustrated, demonstrating that at given points on the fault, rupture direction and slip direction need not be the same. For our model, we introduce a fault with a dip of $60°$, touching a horizontal stope. Some points of interest are marked around it, to represent points where we will compute ground motions. In particular, as the rupture mechanism of the fault will be starting below and progressing upwards, we are especially interested in comparing ground motions of the footwall and the hanging wall. This is illustrated in Figure 12.

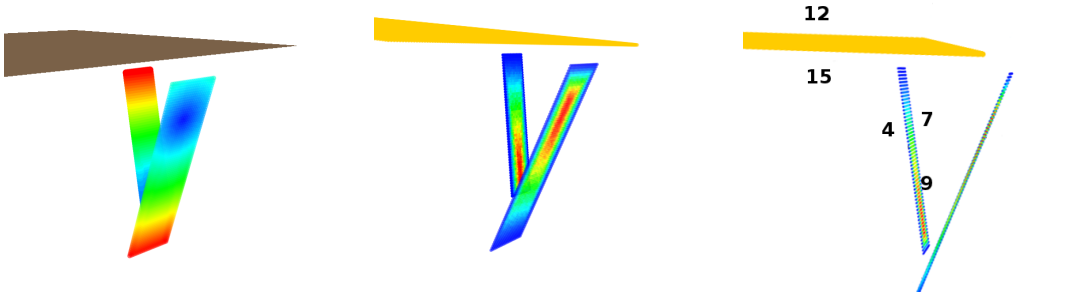

(a) Rupture history of the Ortlepp source, with initiation time per point obtained from radial distance from the focus.

(b) Slip history of the Ortlepp source, with final displacements determined by a k-square distribution.

(c) Synthetic sensor placement around the fault-stope corner.

Figure 12: Comparison of rupture (a) and slip (b) histories for the Ortlepp source. The horizontal structure is a thin tabular stope that can be chosen to intersect the secondary fault. Sensors 4, 7, 9, 11, 12 and 15 (c).

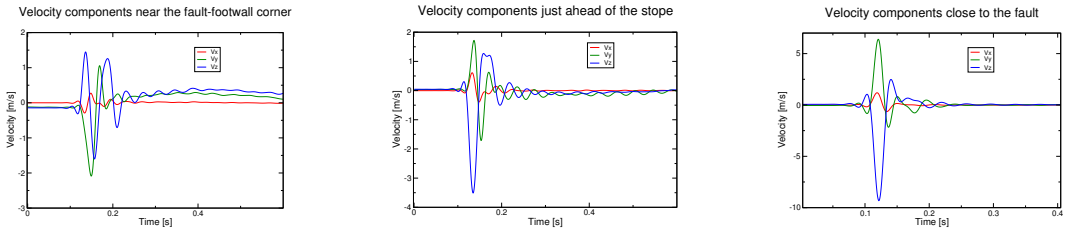

(a) Sensor 4: Velocities near fault and footwall corner

(b) Sensor 7: Velocities just ahead of the stope

(c) Sensor 9: Velocities close to the fault.

Figure 13: Synthetic seismograms recorded around the fault.

After performing the kinematic model run, we investigate the recorded velocity seismograms at sensors 4, 7 and 9 (Figure 13 (a)-(c)). This shows particle velocities close to the fault exceeding 10 m/s at Sensor 9. Both points of interest at Sensors 4 and 7 (which are opposing each other in respectively the footwall and hanging

wall of the fault) experience about 2 m/s velocities, although higher frequency content is observed at Sensor 7 due to interaction of the stope with the wave field.

Figure (14) compares the synthetics of Sensor 12 (hanging wall) that is just above the stope, with that of Sensor 15 (footwall) that is just below the stope.

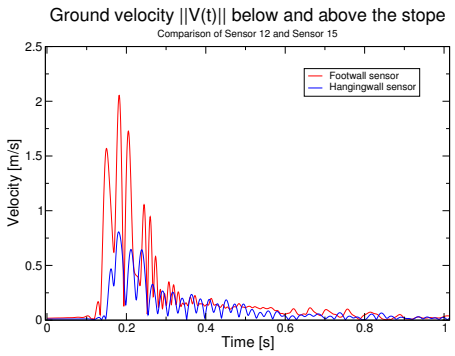

Figure 14: Synthetic seismograms (as absolute velocity) comparing the hanging wall and footwall ground motions of Sensor 12 and 15.

Clearly the footwall sensor records ground motion before the hanging wall sensor due to the shorter distance to source, but additionally as elastic waves need to pass around the stope (modelled as air), the later arrivals at the hanging wall have significantly lower amplitudes. This effect would not have been accurately estimated using routine quick estimates of PGV from ground motion relations that do not take the real material properties of the mine excavation into account.

In Figure 15 shows successive snapshots of the seismic wave field from a two-fault Ortlepp source. In the first few frames, the radiation from the low-potency initial fault is visible, but upon initiation of the second high-potency fault, its contribution to the wave field dominates. When the subsequent waves and the upwards rupture propagation reaches the stope, interaction, reflection and constructive interference can be observed leading to high ground motions.

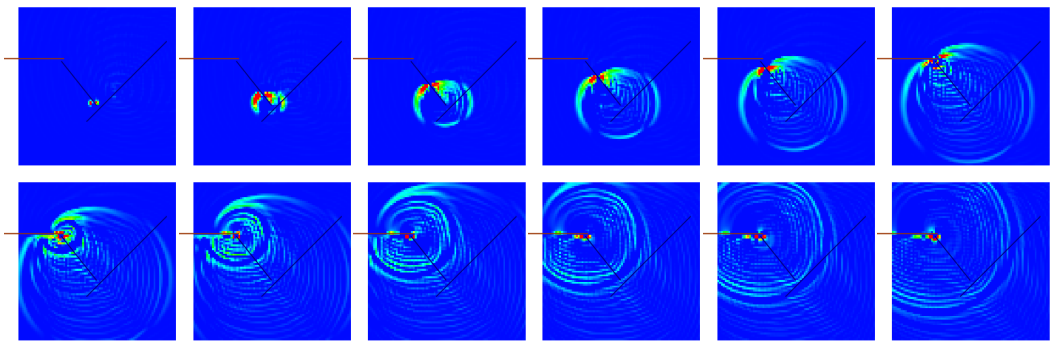

Figure 15: Snapshots of a 2D section of the 3D wave field induced by the synthetic Ortlepp shear event.

3.3 Surface ground motions induced by mining events

Applications of kinematic modelling for mining related problems need not be limited to purely underground scenarios. In this section, we model a hypothetical

event that is induced by rising groundwater in abandoned mines close to a major city.

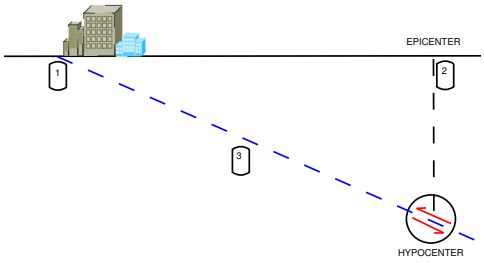

Figure 16: Points of interest at which seismograms are recorded. Sensor 1 is just below the urban area of interest, Sensor 2 at epicenter and Sensor 3 is halfway between the hypocenter and urban city center.

In our model, we choose the event to be 1.5 km below surface, epicentrally 5 km from the major city centre. The event is modelled as a 300 m x 100 m finite elliptical reverse fault with a strike of $0°$, dip of $45°$ and rake of $90°$. Maximum slip velocity is chosen to be 2 m/s and the average displacement over the whole source $\overline{u} = 0.2$ m. We assumed $\log P = 3.5$ and a predominant frequency of 3 Hz.

The model domain is assumed mostly homogeneous with a soil layer of three grid points (spacing of 25m) at the free surface. For the hard rock we choose $\rho = 2700$ kg/m^3, $V_P = 5500$ m/s and $V_S = 3500$ m/s whereas for the 50 m soil layer (which is constructed over the top three grid points in the rock below the air in the finite difference grid) we choose $\rho = 2000$ kg/m^3, $V_P = 4000$ m/s and $V_S = 2000$ m/s. To model the free surface effect and air above it, we choose $\rho = 2000$ kg/m^3, $V_P = 300$ m/s and $V_S = 0$ m/s with high density to avoid stability problems during the kinematic modelling phase on the finite difference grid.

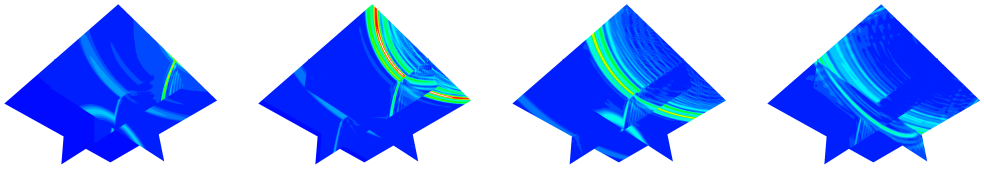

Figure 17: Snapshots of velocity fields during subsequent stages of the kinematic model run of underground event and observed surface ground motions. The intersection of the two vertical sections represents our point of interest, the area below the urban area where damage could potentially occur.

We have computed waveforms in three points of interest indicated at Figure 16. Forward modelling allows us to track velocities and dynamic stresses of the wave field not only at the points of interest, but in the entire model domain. Thus we can simultaneously represent these velocities on multiple planes of interest in subsequent time snapshots. This representation is shown in Figure 17:

With reference to Figure 16, we have recorded synthetic seismograms at Sensors 1-3, and these are shown in Figures 18a, 18b and 18c. For each of these, we show only the vertical component (blue) and the horizontal component (green)

due to our synthetic source being symmetrically aligned in the plane formed by the sensors.

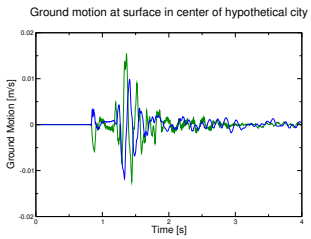

(a) Unfiltered synthetic seismogram at Sensor 1. At surface in the area of interest, both horizontal and vertical ground motions exceeding 15 mm/s are observed, at an observed predominant frequency of 5.8 Hz.

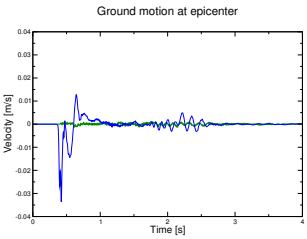

(b) Unfiltered synthetic seismogram at Sensor 2. Significant vertical ground motion is observed, resulting in (after integrating to displacement) permanent displacement of over 1 mm.

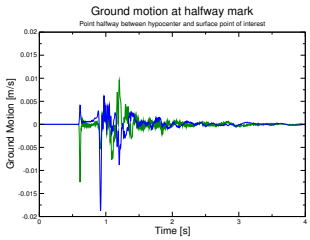

(c) Unfiltered synthetic seismogram at Sensor 3. Here the initial arrivals and their immediate coda are clear of reflected waves, as this synthetic recording is underground, halfway between the hypocenter and point of interest on surface.

Figure 18: Synthetics at three points in the simulation of ground motions near surface. The predominant frequency at Sensor 1 was calculated by computing a power spectrum over the two non-trivial components of the observed waveform. The energy of the ripple observed at Sensor 2 at around 2s is 10 Hz (taken as average over 8 consecutive full periods). While potentially a numerical effect this can be compared to the expected horizontal S wave resonance (20 Hz) and expected vertical S wave resonance (10 Hz).

At Sensor 2 (Figure 18b) significant vertical ground motions are observed, but are not expected to be particularly damaging to surface structures. By virtue of the displacement curve obtained by integrating this velocity time series, there is clearly an upwards permanent displacement of the surface at this sensor, which corresponds with what is to be expected of reverse faulting (Figure 16). The stronger horizontal ground motions at Sensor 1 (Figure 18a) which are actually further from the hypocenter are expected to have a more damaging effect.

Acknowledgment

This work is a part of the Mine Seismology Research Programme of the Institute of Mine Seismology for 2011/12 sponsored by Anglo American Platinum South Africa, Anglo Gold Ashanti South Africa, BHP Billiton Nickel West Australia, El Teniente Chile, Gold Fields South Africa, Harmony South Africa, LKAB Sweden and Newcrest Mining Australia. We thank two anonymous reviewers and Riaan Carstens of AngloPlatinum for their constructive comments, which improved the manuscript.

References

Andrews, D. J. (1976), Rupture velocity of plane strain shear cracks, *Journal of Geophysical Research*, *81*(32), 5679–5687.

Andrews, D. J., T. C. Hanks, and J. W. Whitney (2007), Physical limits on ground motion at Yucca Mountain, *Bulletin of the Seismological Society of America*, *97*(6), 1771–1792.

Archuleta, R. J. (1984), A faulting model for the 1979 Imperial Valley earthquake, *Journal of Geophysical Research*, *89*(B6), 4559–4585.

Ben-Zion, Y., and L. Zhu (2002), Potency-magnitude scaling relation for southern California earthquakes with 1.0<M<7.0, *Geophysical Journal International*, *148*, F1–F5.

Benjamin, J. R. (1968), Probabilistic model for seismic force design, *Journal of Structural Engineering ASCE*, *94 (ST5)*, 1175–1196.

Beresnev, I., and G. M. Atkinson (1997), Modeling finite-fault radiation from the omega-n spectrum, *Bulletin of the Seismological Society of America*, *87*(1), 67–84.

Brune, J. N. (1970), Tectonic stress and the spectra of seismic shear waves from earthquakes, *Journal of Geophysical Research*, *75*(26), 4997–5009.

Burridge, R. (1969), The numerical solution of certain integral equations with non-integrable kernels arising in the theory of crack propagation and elastic wave diffraction, *Phil. Trans. Roy. Soc. London*, *A 265*, 353–381.

Burridge, R. (1973), Admissible speeds for plane-strain self-similar shear cracks with friction but lacking cohesion, *Geophys. J. R. Astron. Soc.*, *35*(4), 439–455.

Campbell, K. W. (1982), Bayesian analysis of extreme earthquake occurrences. Part 1: Probabilistic hazard model, *Bulletin of the Seismological Society of America*, *72*(5), 1689–1705.

Capes, G. (2010), Seismic experience at the Newcrest Mining Limited - Ridgeway Gold Mine, in *Institute of Mine Seismology 2010 Seminar, Western Levels, South Africa - Electronic Proceedings*, edited by A. J. Mendecki.

Chandler, K. N. (1952), The distribution and frequency of record values, *Journal of the Royal Statistical Society, Series B (Methodological)*, *14*(2), 220–228.

Clayton, R., and B. Engquist (1977), Absorbing boundary conditions for acoustic and elastic wave equations, *Bulletin of the Seismological Society of America*, *67*(6), 1529–1540.

Cooke, P. (1979), Statistical inference for bounds of random variables, *Biometrica*, *66*(2), 367–374.

Cranswick, E. (2011), How many earthquakes are caused by mining in Australia, in *Proceedings of the 2011 IUGG Conference, Melbourne*, IASPEI.

Dunham, E. M. (2007), Conditions governing the occurrence of supershear ruptures under slip-weakening friction, *Journal of Geophysical Research*, *112*(B07302), 1–24, doi:10.1029/2006JB004717.

Durrheim, R. J., R. L. Anderson, A. Cichowicz, R. Ebrahim-Trollope, G. Hubert, A. Kijko, A. McGarr, W. D. Ortlepp, and N. van der Merwe (2006), Investigation into the risks to miners, mines, and the public associated with large seismic events in gold mining districts, *Expert opinion*, Department of Mineral and Energy of South Africa.

Gibowicz, S. J. (1975), Variation of source properties: The Inangahua, New Zealand, aftershocks of 1968, *Bulletin of the Seismological Society of America*, *65*(1), 261–276.

Gibowicz, S. J., Z. Droste, B. Guterch, and J. Hordejuk (1981), The Belchatow, Poland, earthquakes of 1979 and 1980 induced by surface mining, *Engineering Geology*, *17*, 257–271.

Gibson, G., V. Wesson, and K. McCue (1990), The Newcastle earthquake aftershock and its implications, in *Proceedings of the Conference on the Newcastle Earthquake, Newcastle*, pp. 14–18.

Glick, N. (1978), Breaking records and breaking boards, *The American Mathematical Monthly*, *85*(1), 2–26.

Graves, R. W. (1996), Simulating seismic wave propagation in 3D elastic media using staggered grid finite differences, *Bulletin of the Seismological Society of America*, *86*(4), 1091–1106.

Handley, M. F., J. A. J. de Lange, F. Essrich, and J. A. Banning (2000), A review of the sequential grid mining method employed at Elandsrand Gold Mine, *The Journal of The Southern African Institute of Mining and Metallurgy*, *100*(3), 157–168.

Hao, H. (2010), Reconnaissance report of structural damage in the Kalgoorlie-Boulder area, *Tech. rep.*, AEES Newsletter, May.

Herrero, A., and P. Bernard (1994), A kinematic self-similar rupture process for earthquakes, *Bulletin of the Seismological Society of America*, *84*(4), 1216–1228.

Ida, Y. (1973), The maximum acceleration of seismic ground motion, *Bulletin of the Seismological Society of America*, *63*(3), 959–968.

Kanamori, H. (1972), Determination of effective tectonic stress associated with earthquake faulting. The Tottori earthquake of 1943, *Physics of the Earth and Planetary Interiors*, *5*, 426–434.

Kanamori, H., and D. L. Anderson (1975), Theoretical basis of some empirical relations in seismology, *Bulletin of the Seismological Society of America,*, *65*(5), 1073–1095.

Kijko, A. (2004), Estimation of the maximum earthquake magnitude, Mmax, *Pure and Applied Geophysics*, *161*(8), 1655–1681, doi:10.1007/s00024-004-2531-4.

Klose, C. D. (2007), Geomechanical modeling of the nucleation process of Australia's 1989 M5.6 Newcastle earthquake, *Earth and Planetary Science Letters*, *256*(3-4), 547–553, doi:10.1016/j.epsl.2007.02.009.

Knopoff, L., and Y.-T. Chen (2000), Frictional sliding, shock waves, and granular rotations, in *Proceedings 2nd ACES Workshop in Japan*.

Lu, X., A. J. Rosakis, and N. Lapusta (2010), Rupture modes in laboratory earthquakes: Effect of fault prestress and nucleation conditions, *Journal of Geophysical Research*, *115*(B12302), 1–25, doi:10.1029/2009JB006833.

Malan, D. F. (1999), Time-dependent behaviour of deep level tabular excavations in hard rock, *Rock Mechanics and Rock Engineering*, *32*(2), 123–155.

McGarr, A., and J. B. Fletcher (2001), A method for mapping apparent stress and energy radiation applied to the 1994 Northridge Earthquake Fault Zone-Revisited, *Geophysical Research Letters*, *28*(18), 3529–3532, doi:10.1029/2001GL013094.

McGuire, R. K. (1977), Effects of uncertainty in seismicity on estimates of seismic hazard for the east coast of the United States, *Bulletin of the Seismological Society of America*, *67*(3), 827–848.

Mendecki, A. J. (1993), Real time quantitative seismology in mines: Keynote Address, in *Proceedings 3rd International Symposium on Rockbursts and Seismicity in Mines, Kingston, Ontario, Canada*, edited by R. P. Young, pp. 287–295, Balkema, Rotterdam.

Mendecki, A. J. (2005), Persistence of seismic rock mass response to mining, in *Proceedings 6th International Symposium on Rockburst and Seismicity in Mines, Perth, Australia*, edited by Y. Potvin and M. R. Hudyma, pp. 97–105, Australian Centre for Geomechanics.

Mendecki, A. J. (2008), Forecasting seismic hazard in mines, in *Proceedings 1st Southern Hemisphere International Rock Mechanics Symposium, Perth, Australia*, edited by Y. Potvin, J. Carter, A. Diskin, and R. Jeffrey, pp. 55–69, Australian Centre for Geomechanics.

Nicolis, G., and I. Prigogine (1989), *Exploring Complexity*, W. H. Freeman and Company, New York.

Olson, A. H., and R. J. Apsel (1982), Finite faults and inverse theory with applications to the 1979 Imperial Valley earthquake, *Bulletin of the Seismological Society of America*, *72*(6), 1969–2001.

Ortlepp, W. D. (1984), Rockbursts in South African gold mines: A phenomenological view, in *Proceedings 1st International Symposium on Rockbursts and Seismicity in Mines, Johannesburg, South Africa*, edited by N. C. Gay and E. H. Wainwright, pp. 165–178, South African Institute of Mining and Metallurgy.

Ortlepp, W. D. (1997), *Rock Fracture and Rockbursts - An Illustrative Study*, Monograph Series M9, 126 pp., South Afican Institute of Mining and Metallurgy.

Ortlepp, W. D. (2006), Comment on the paper: Strong ground motion and site response in deep south african mines by AM Milev, SM Spottiswood, *The Journal of The Southern African Institute of Mining and Metallurgy*, *106*(8), 593–597.

Ortlepp, W. D., R. Armstrong, J. A. Ryder, and D. O'Connor (2005), Fundamental study of micro-fracturing on the slip surface of mine-induced dynamic brittle shear zones, in *6th International Symposium on Rockburst and Seismicity in Mines*, edited by Y. Potvin and M. Hudyma, pp. 229–237.

Robson, D. S., and J. H. Whitlock (1964), Estimation of a truncation point, *Biometrica*, *51*(1-2), 33–39.

Rundle, J. B., K. F. Tiampo, W. Klein, and J. S. S. Martins (2002), Self-organization in leaky threshold systems: The influence of near-mean field dynamics and its implications for earthquakes, neurobiology, and forecasting, *PNAS*, *19*(1), 2514–2521.

Saenger, E., and T. Bohlen (2004), Finite-difference modeling of viscoelastic and anisotropic wave propagation using the rotated staggered grid, *Geophysics*, *69*, 583–591.

Sammis, C. G., and Y. Ben-Zion (2008), Mechanics of grain-size reduction in fault zones, *Journal of Geophysical Research*, *113*(B02306), 1–12, doi:10.1029/2006JB004892.

Savage, J. C. (1971), Radiation from supersonic faulting, *Bulletin of the Seismological Society of America*, *61*(4), 1009–1012.

Somerville, P., et al. (1999), Characterizing crustal earthquake slip models for the prediction of strong ground motion, *Seismological Research Letters*, *70*(1), 59–80.

Sornette, D. (2005), Statistical physics of rupture in heterogeneous media, in *Handbook of Materials Modeling*, vol. 1, edited by S. Yip, chap. Article 4.4, Springer Science and Business Media.

Spudich, P., and E. Cranswick (1984), Direct observation of rupture propagation during the 1979 Imperial Valley earthquake using a short baseline accelerometer array, *Bulletin of the Seismological Society of America*, *74*(6), 2083–2114.

Van Aalsburg, J., W. I. Newman, D. L. Turcotte, and J. B. Rundle (2010), Record-breaking earthquakes, *Bulletin of the Seismological Society of America*, *100*(4), 1800–1805.

Van Aswegen, G. (1990), Fault stability in SA gold mines., in *Proceedings of the International Conference on Mechanics of Jointed and Faulted Rock, Vienna*, edited by P. Rossmanith.

van Aswegen, G., and A. J. Mendecki (1999), Mine layout, geological features and seismic hazard, *Final report gap 303*, Safety in Mines Research Advisory Committee, South Africa.

Weertman, J. (1969), Dislocation motion on an interface with friction that is dependent on sliding velocity, *Journal of Geophysical Research*, *74*(27), 6617–6622.

Wesnousky, S. G. (1999), Crustal deformation processes and the stability of the Gutenberg-Richter relationship, *Bulletin of the Seismological Society of America*, *89*(4), 1131–1137.

Yuan, F., V. Prakash, and T. Tullis (2011), Origin of pulverized rocks during earthquake fault rupture, *Journal of Geophysical Research*, *116*(B06309), 1–18, doi:10.1029/2010JB007721.